

Measurement of the hyperfine splitting of the $6S_{1/2}$ level in rubidium.

A. Pérez Galván, Y. Zhao, L. A. Orozco¹

¹*Joint Quantum Institute, Department of Physics,*

University of Maryland and National Institute of Standards and Technology, College Park, MD 20742-4100, USA.

(Dated: October 30, 2018)

We present a measurement of the hyperfine splitting of the $6S_{1/2}$ excited level of rubidium using two photon absorption spectroscopy in a glass cell. The values we obtain for the magnetic dipole constant A are 239.18(03) MHz and 807.66(08) MHz for ^{85}Rb and ^{87}Rb , respectively. The combination of the magnetic moments of the two isotopes and our measurements show a hyperfine anomaly in this atomic excited state. The observed hyperfine anomaly difference has a value of ${}_{87}\delta_{85} = -0.0036(2)$ due to the finite distribution of nuclear magnetization, the Bohr-Weisskopf effect.

PACS numbers: 32.10.Fn, 32.30.-r, 21.60.-n

I. INTRODUCTION

Precise measurements of hyperfine splittings of the ground and excited states are necessary to explore the complete dynamics of the electron cloud-nucleus interaction in the atom. New experimental approaches such as femtosecond frequency combs and small linewidth lasers together with laser cooling and trapping reach now increased accuracy for high precision studies of hyperfine structure in excited levels [1, 2, 3, 4, 5]. This new wave of experiments has renewed the interest of theorists in predicting accurate electron-nucleus interactions. These calculations of hyperfine splittings in excited states, where electron correlations are less complicated, are more sensitive to nuclear structure details [6].

Measurements of hyperfine splittings are also of interest to the atomic parity non-conservation (PNC) community. Experiments of atomic PNC rely heavily on calculations of operator expectation values to extract from the experimental data information on the weak interaction. The accuracy of the calculations is gauged against expectations values of atomic properties such as energy levels, ionization energy, electric dipole operators of the electronic levels, fine and hyperfine splittings. The hyperfine splitting measurements, in particular, represent ideal benchmarks for the *ab initio* calculations of the electronic wave function at distances close to the nucleus [7, 8]. Currently, the PNC *ab initio* calculations of theoretical groups using many body perturbation theory (MBPT) have reached a precision better than 1% [9, 10, 11].

We present in this paper the details of the measurement of the hyperfine splitting of the $6S_{1/2}$ excited level in ^{85}Rb and ^{87}Rb [12]. We perform the experiment in a glass cell with rubidium vapor with natural isotopic abundances under a controlled environment. We observe in our experimental data deviations from the assumed point interaction between the valence electron and the nucleus *i.e.* a hyperfine anomaly, and find that a change in the distribution of the nuclear magnetization between isotopes explains the observation.

The organization of the paper is as follows: section II

gives the theoretical background, section III contains the methodology and experimental setup as well as the studies of possible systematic errors and results. Section IV shows the comparison with theory and section V contains the conclusions.

II. THEORETICAL BACKGROUND

Pauli suggested in 1924 that the “hyperfine” splittings observed in very precise spectroscopic studies of fine structure in atoms were due to the interaction between the atomic electrons and the magnetic moment of the nucleus [13]. Three years later Back and Goudsmit succeeded in analyzing the very small splittings of bismuth using the assumption of Pauli and the coupling of angular momenta [14, 15]. Theoretical predictions of the splittings were moderately successful in explaining the size of the experimental findings, mainly due to the complexity of the relativistic many-electron system. However, in the last twenty years there has been an exceptional output of very accurate theoretical results coming from MBPT culminating in the extraction of weak interaction couplings from the atomic PNC measurement in Cs [16, 17]. There are currently proposals to perform a complementary PNC measurement in francium where calculations of atomic properties are reaching the precision of those in cesium [18].

A. Hyperfine splitting

Although a complete treatment requires a full relativistic theory, estimations of the interplay between the nuclear moments and the electromagnetic fields created by the electron following classical electrodynamics agree with the experimental results and provide physical insight of the phenomenon (see for example Refs.[19, 20]). We follow this approach in the discussion below. The interested reader should consult Ref. [21] for a relativistic derivation.

Two types of nucleus-electron interactions suffice to account for the hyperfine splitting in most atoms. The largest of the contributions comes from the nuclear magnetic dipole coupling to the magnetic field created by the electrons at the nucleus. The second one arises from the interaction between the nuclear electric quadrupole and the gradient of the electric field generated by the electrons at the nucleus. The latter vanishes for spherically symmetric charge distributions which correspond to electronic angular momentum J equal to 0 or 1/2. The hyperfine energy shift E_{HF} for these levels is [20]:

$$E_{HF} = \frac{A}{2}(F(F+1) - I(I+1) - J(J+1)), \quad (1)$$

where F is the total angular momentum, I is the nuclear spin and A is the magnetic dipole interaction constant. The derivation of A for a hydrogen-like atom by Fermi and Segrè assumes a point nuclear magnetic dipole [19]

$$A_{point} = \frac{16\pi}{3} \frac{\mu_0}{4\pi\hbar} g_I \mu_N \mu_B |\psi(0)|^2, \quad (2)$$

where $\psi(0)$ is the electronic wave function evaluated at the nucleus, μ_B is the Bohr magneton, μ_N is the nuclear magneton and g_I is the nuclear gyromagnetic factor.

The nuclear magnetic dipole acquires an extra potential energy under an external DC magnetic field. For small values of the field ($g_F \mu_B B / E_{HF} \ll 1$) F is a good quantum number and the energy of the system is given by

$$E_{HF}(B) = E_{HF}(0) + g_F \mu_B m_F B, \quad (3)$$

where g_F is the total g-factor, m_F is the magnetic quantum number, B is the magnetic field and $E_{HF}(0)$ is the value of the energy at zero magnetic field. In this regime of small splittings compared to $E_{HF}(0)$, g_F is given by:

$$g_F = g_J \frac{F(F+1) + J(J+1) - I(I+1)}{2F(F+1)} - g_I \frac{F(F+1) + I(I+1) - J(J+1)}{2F(F+1)},$$

where g_J is the electronic g-factor.

B. *Ab initio* calculations

Hyperfine interactions represent a formidable many body problem. A thorough study must approach the problem from a relativistic standpoint which further complicates the interactions in a multi-electron atom. In recent years relativistic MBPT has shown itself to be a powerful and systematic way of extracting, from the high quality wave functions that it generates, precise atomic properties such as hyperfine splittings [11, 22].

The full method is outlined in Ref.[23] and references therein. Briefly, the method, applied to alkali atoms, consists of evaluating a no-pair relativistic Hamiltonian with

Coulomb interactions with a frozen core Dirac-Hartree-Fock wave function of a one valence electron atom. The Hamiltonian includes projection operators to positive energy states of the Dirac Hamiltonian. Their presence gives normalizable, bound state solutions. The wave function contains single and double excitations to all orders; these correspond to wave functions useful for calculating energy levels and transition matrix elements. In order to calculate accurate hyperfine constants a set of triple excitations has to be added. The evaluation of the wave function yields coupled equations that are solved iteratively for the excitation coefficients which are then used to obtain atomic properties.

The calculations of the hyperfine constants are corrected for the finite size of the nuclear magnetic moment up to zeroth order only due to their small size in the lighter alkalis (Na, K, Rb). In cesium and francium the correction becomes more important and is included to all orders. The calculation ignores isotopic changes of the magnetization distribution and it is modeled as a uniformly magnetized sphere for all the atoms. The magnetization radius used is equal to the charge radius and the neutron skin contribution is ignored.

C. Hyperfine anomalies

The atomic electron sees the nucleus, most of the time, as a structureless entity with a single relevant parameter, its charge Z . We should expect the electronic wave functions of different isotopes, to a very good approximation, to be the same. It follows then, using Eq. 2 that

$$\frac{A_{point}^{87}}{A_{point}^{85}} = \frac{g_I^{87}}{g_I^{85}}, \quad (4)$$

where the superindex denotes the atomic number of the isotope.

However, high precision experiments show differences or anomalies from this description. It is necessary to consider the nucleus as an extended, structured object with specific finite magnetization and electric charge distributions for each isotope. We can express the anomaly by writing the magnetic dipole constant of an extended nucleus A_{ext} as a small correction to A_{point} [19]

$$A_{ext} = A_{point} f_R (1 + \epsilon_{BCRS}) (1 + \epsilon_{BW}), \quad (5)$$

where f_R represents the relativistic correction. The last two terms in parenthesis modify the hyperfine interaction to account for an extended nucleus. The Breit-Crawford-Rosenthal-Schawlow (BCRS) correction [24, 25, 26], the largest of the two, modifies the electronic wave function inside the nucleus as a function of the specific details of the nuclear charge distribution. The second one, the Bohr-Weisskopf (BW) correction [27], describes the influence on the hyperfine interaction of finite space distribution of the nuclear magnetization.

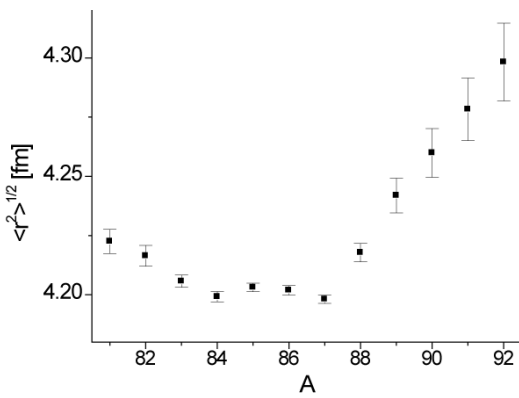


FIG. 1: Plot of nuclear charge radius of rubidium as a function of atomic number. Adapted from Ref. [30].

Direct extraction of hyperfine anomalies from the experimental data requires theoretical knowledge of both hyperfine structure constants and magnetic moments. However, the anomalies can still be observed from the measurements of the magnetic dipole constants in different isotopes and the values of the g -factors [28, 29]. Deviations from Eq. 4 are expressed in terms of the hyperfine anomaly difference ${}_{87}\delta_{85}$:

$$\frac{A^{87}g_I^{85}}{A^{85}g_I^{87}} \cong 1 + {}_{87}\delta_{85}, \quad (6)$$

with ${}_{87}\delta_{85} = \epsilon_{BW}^{87} - \epsilon_{BW}^{85} + \epsilon_{BCRS}^{87} - \epsilon_{BCRS}^{85}$. $A {}_{87}\delta_{85} \neq 0$ indicates the presence of a hyperfine anomaly.

1. Breit-Crawford-Rosenthal-Schawlow effect

The interaction between an electron and an atomic nucleus is precisely described by the Coulomb potential when both of them are far away from each other, no matter whether the nucleus is a point or an extended source. For interactions that require the nucleus and the electron to be at close distances, such as the hyperfine interaction, an $1/r$ potential is no longer adequate. The correction to the electronic wave function due to the modified nuclear potential is known as the Breit-Crawford-Rosenthal-Schawlow correction.

Calculations of ϵ_{BCRS} take into consideration how the charge is distributed over the nucleus. Rosenthal and Breit considered for their calculation the charge to be on the surface of the nucleus [24]. Schawlow and Crawford also calculated the change of the wave function except they considered the charge to be uniformly distributed in the nucleus [25]. Rosenberg and Stroke proposed later on a third model to improve the agreement between theory and experiment: a diffuse nuclear charge distribution [26].

The neutron and proton shells in rubidium determine the deformation as well as the spatial distribution of the

nuclear charge. The neutron shell for ${}^{87}\text{Rb}$ is closed at magic number $N = 50$ making it impervious to the addition and subtraction of nuclear matter [30, 31]. The subtraction of two neutrons to form ${}^{85}\text{Rb}$ does not affect significantly the electric charge distribution, and the electric potential, compared to the one from ${}^{87}\text{Rb}$, remains the same (see Fig. 1).

The expression of ϵ_{BCRS} for the uniformly charged sphere and charge on surface models is [21]:

$$\epsilon_{BCRS} = \frac{2(\kappa + \rho)\rho(2\rho + 1)}{(2\kappa + 1)(\Gamma(2\rho + 1))^2} \left(\frac{pZr_N}{a_0} \right)^{2\rho-1}, \quad (7)$$

where p is a constant of order unity, $\rho = \sqrt{\kappa^2 - (Z\alpha)^2}$, a_0 and α are the Bohr radius and electromagnetic coupling constant, respectively, r_N is the nuclear radius, and κ is related to the electronic angular momentum through the equation $\kappa = 1 + J(J + 1) - L(L + 1) - S(S + 1)$. Table I shows the value of the correction for a uniformly distributed charge as well as the nuclear radius of each isotope employed in the calculation.

| | r_N [fm] | Ref. | ϵ_{BCRS} |
|--------------------|------------|------|-------------------|
| ${}^{85}\text{Rb}$ | 4.2031(18) | [30] | 0.0090835(34) |
| ${}^{87}\text{Rb}$ | 4.1981(17) | [30] | 0.0090735(36) |

TABLE I: Values of ϵ_{BCRS} and corresponding nuclear radius for both rubidium isotopes.

Rosenfeld and Stroke propose a trapezoidal charge distribution to approximate their model. The interested reader should consult Ref. [26] for further explanation. All three models give relatively large ϵ_{BCRS} ($\sim 1\%$), however, the difference between both isotopes for all models is very small: $\epsilon_{BCRS}^{87} - \epsilon_{BCRS}^{85} \sim 10^{-5}$.

2. Bohr-Weisskopf effect

The interplay between nuclear magnetization with the magnetic field created by the atomic electrons causes the hyperfine splitting in atoms. A natural extension of hyperfine splitting measurements is to compare models of nuclear magnetism.

Nuclear magnetization is described in terms of nuclear moments with the biggest contribution coming from the nuclear magnetic dipole moment. The assumption of a point magnetic dipole gives good agreement between calculations and experiment, however it does not provide the complete picture. Nuclear magnetization has a finite volume. The electron wavefunctions of levels with total angular momentum $J = 1/2$ have a bigger overlap with the nucleus and are able to experience the subtle changes of the spatial distribution of the nuclear magnetization. This wave functions need to be modified to correctly account for the hyperfine splitting.

The corrections ϵ_{BW} to the wave functions due to a finite magnetization distribution were first computed by

Bohr and Weisskopf [27]. They assumed a uniformly distributed magnetization over the nucleus for their calculation with a predicted $\epsilon_{BW}^{87} - \epsilon_{BW}^{85}$ that ranges between 0.11% and 0.29%. The BW correction roughly scales as [27]:

$$\epsilon_{BW} \sim \left(\frac{Zr_N}{a_0}\right) \left(\frac{a_0}{2Zr_N}\right)^{2(1-\sqrt{1-(Z\alpha)^2})} \left(\frac{r^2}{r_N^2}\right)_{Av}, \quad (8)$$

where the average is taken over the magnetization distribution, with $(r^2/r_N^2)_{Av} = 3/5$ for a uniform magnetization. For rubidium this gives a correction of the order of 0.2%, however it is strongly dependent on spin and orbital states of the nucleons i.e. on the specifics of the nuclear magnetization. Stroke *et. al.* performed the same calculation using a trapezoidal magnetization distribution [32]. Their results agree very well with experimental information extracted from the ground state; they calculate a hyperfine anomaly difference of 0.33%. Both of these results are independent for the main quantum number of the valence electron [19].

The nuclear shell model predicts that the total magnetic dipole moment has contributions from both the proton and the neutron shell, each with orbital and spin angular momenta [19]

$$\vec{\mu} = \sum_{i=n,p} (g_{s,i}^{eff} \vec{s}_i + g_{l,i}^{eff} \vec{l}_i) \mu_N, \quad (9)$$

where g_s^{eff} and g_l^{eff} are the effective nuclear spin and nuclear orbital gyromagnetic ratios, respectively, \vec{s} and \vec{l} are the nuclear spin and nuclear orbital angular momenta and the sum is taken over both shells. The g -factors have the values $g_s^{eff}=3.1(2)$ and $g_l^{eff}=1.09(2)$ [33].

The magnetic dipole moment in rubidium comes almost entirely from the vector addition of the orbital and spin angular momenta of a single valence proton. The neutron shell is almost spherical for both isotopes due to its closed shell structure and the contribution to the angular momentum from the neutron shell is very small.

The lighter of the two isotopes, ^{85}Rb , has the valence proton in an almost degenerate f orbital with its spin and orbital momenta antialigned yielding a value of $I=5/2$. Adding two more neutrons to the core shifts the energy level of the valence proton to the nearby p orbital and aligns both momenta giving the known value of $I=3/2$. Table II presents the theoretical prediction of the nuclear magnetic moment using Eq. 9 as well as the experimental result. It is indeed remarkable that such a simple model reproduces closely the experimental results, particularly for the closed nuclear shell structure of ^{87}Rb .

Three main factors make the two stable isotopes of rubidium good candidates for observing the BW effect: First the different orientation of the nuclear spin of the valence proton with respect to the nuclear orbital angular momentum. Second, the small relative difference in nuclear charge deformation. Third, the change of orbital for the valence proton in the two isotopes.

| | Theory [μ_N] | Experiment [μ_N] | Ref. |
|------------------|--------------------|------------------------|------|
| ^{85}Rb | 2.00 | 1.35298(10) | [34] |
| ^{87}Rb | 2.64 | 2.75131(12) | [34] |

TABLE II: Theoretical and experimental values of the nuclear dipole moment for rubidium.

D. Two-photon spectroscopy

We use atomic laser spectroscopy to measure the hyperfine splitting in two isotopes of rubidium. Parity requires a two photon electric dipole transition to reach the $6S_{1/2}$ state from the $5S_{1/2}$ ground state. We increase the probability of transition by using the $5P_{1/2}$ level as an intermediate step. We develop a theoretical model of the two-photon transition that includes the main physical aspects of our atomic system (see Fig. 2) based on a density matrix formalism.

Our experimental setup consists of two counter propagating laser beams going through a glass cell with rubidium vapor in a small magnetic field. We lock the laser at 795 nm on resonance, the middle step to the $5P_{1/2}$ level, while we scan the 1.324 μm laser (from here on referred to as the 1.3 μm laser) over the $6S_{1/2}$ level and observe the absorption of the 795 nm laser. The system can be modeled as a three level atom in which the on-resonance middle step enhances the excitation to the final step and the counter propagating laser beams help suppress the Doppler background (see for example Ref. [35]). However, numerical simulations show that we have to model our system as a five level atom to include its main qualitative feature: optical pumping effects increase the absorption of the 795 nm laser when the 1.3 μm laser is on resonance.

Figure 3 shows our simplified atomic model. We have neglected the Doppler effects as well as the Zeeman sub-levels in order to keep the calculation as simple as possible without losing the main qualitative features of our system. Level $|1\rangle$ represents the lower hyperfine state of

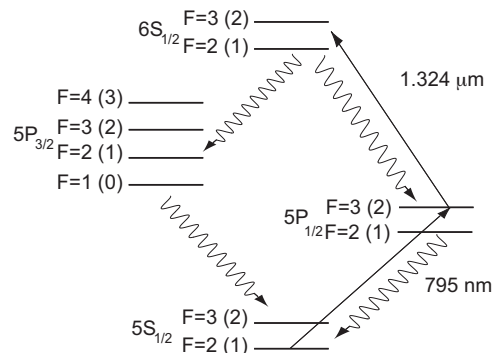


FIG. 2: Energy levels relevant to our experiment (energy separations not drawn to scale). The numbers correspond to ^{85}Rb (^{87}Rb). Straight arrows correspond to the excitation lasers, undulated arrows to decays.

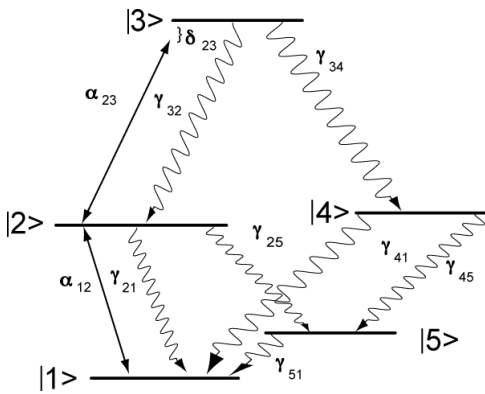


FIG. 3: Energy level diagram of the theoretical model representing our system. The $\gamma_{i,j}$ corresponds to the decay rate between levels $|i\rangle$, $|j\rangle$, $\alpha_{i,j}$ is the Rabi frequency relating levels $|i\rangle$ and $|j\rangle$, and δ_{23} is the detuning from resonance of the excitation laser between levels $|2\rangle$ and $|3\rangle$.

the $5S_{1/2}$ level while $|2\rangle$ is the upper hyperfine state of the $5P_{1/2}$. The decay rate between the two levels is $\gamma_{21}/2\pi = 6$ MHz [36]. We simplify the hyperfine states of the $6S_{1/2}$ level to just one level with decay rate $\gamma_{32}/2\pi = 3.5$ MHz [37]. The ground and intermediate levels are coupled by the Rabi frequency α_{12} while the intermediate and the excited levels are coupled by α_{23} . The remaining two levels, $|4\rangle$ and $|5\rangle$, represent all other decay channels out of the cascade system and the upper hyperfine ground level, respectively. The detuning between levels $|1\rangle$ and $|2\rangle$ is zero for our experiment, but we let the detuning between levels $|2\rangle$ and $|3\rangle$ vary as δ_{23} . The total population is normalized to one.

We are left with a set of twenty five linear equations for the slowly varying elements of the density matrix σ_{nm} after using the rotating wave approximation. These are

$$\begin{aligned} & \sum_k (\gamma_{kn}\sigma_{kk} - \gamma_{nk}\sigma_{nn}) + \\ & \frac{i}{2} \sum_k (\alpha_{nk}\sigma_{kn} - \sigma_{nk}\alpha_{kn}) = 0 \text{ for } n = m, \\ & [i(\Omega_{nm} - \omega_{nm}) - \Gamma_{nm}] \sigma_{nm} + \\ & \frac{i}{2} \sum_k (\alpha_{nk}\sigma_{km} - \sigma_{nk}\alpha_{km}) = 0 \text{ for } n \neq m, \end{aligned}$$

where $\omega_{nm} = (E_n - E_m)/\hbar$ is the transition frequency, $\Omega_{nm} = -\Omega_{mn}$ is the laser frequency connecting the levels. The damping rate is given by:

$$\Gamma_{nm} = \frac{1}{2} \sum_k (\gamma_{nk} + \gamma_{mk}).$$

We solve for σ_{12} leaving the detuning between levels $|2\rangle$ and $|3\rangle$ ($\delta_{23} = \Omega_{23} - \omega_{23}$) as a free parameter. We plot the negative of the imaginary part of σ_{12} , which is proportional to the absorption of level $|2\rangle$, as a function of δ_{23} for several different sets of parameters. Our five level

model reproduces the increase of absorption observed as the second excitation goes into resonance. This can be explained in the following way. The laser coupling levels $|1\rangle$ and $|2\rangle$, in the absence of the second excitation, pumps the atoms to level $|5\rangle$. On steady state there will be little absorption due to a very small amount of atoms being transferred from $|5\rangle$ to $|1\rangle$. By adding the second excitation a new reservoir of “fresh” unexcited atoms appears in level $|1\rangle$. Instead of falling to the non-absorbing level $|5\rangle$, they travel to level $|3\rangle$ and then decay to the initial ground state level through level $|4\rangle$. These “fresh” atoms will add to the ground state population and increase the absorption.

Figure 4 shows samples of our simulation. We have plotted the absorption of the laser connecting levels $|1\rangle$ and $|2\rangle$ as a function of the detuning of the second laser. Figure 4 (a) shows how the absorption increases as the second laser goes on resonance while Fig. 4 (b) shows a decrease. Both plots have the same model parameters except for the ratio γ_{41}/γ_{45} . This ratio determines whether the atom will be lost or return to the cycle. A ratio bigger than one pumps atoms preferentially to level $|1\rangle$ rather than level $|5\rangle$ which constitutes a fresh reservoir of excitable atoms.

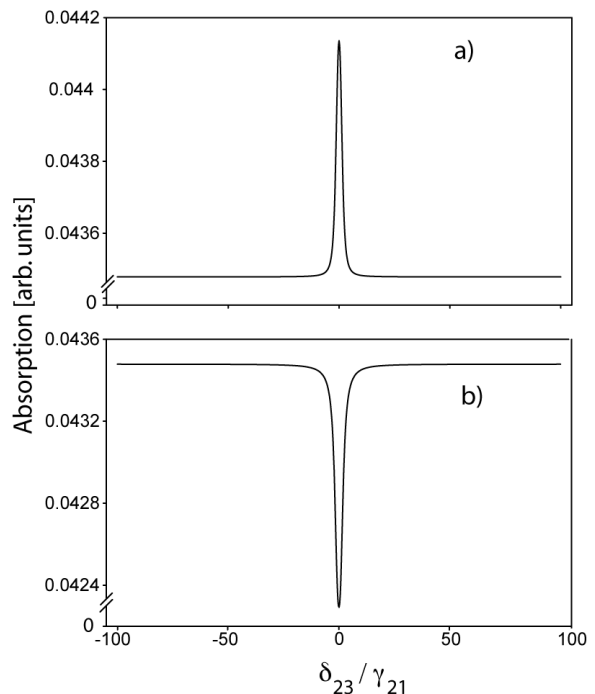


FIG. 4: Numerical simulation of the absorption of the 795 nm laser as a function of the normalized detuning of the $1.3 \mu\text{m}$ laser to level $|3\rangle$ in units of γ_{21} . Both plots have the same parameters except for the ratio γ_{41}/γ_{45} . (a) Increase of absorption with $\gamma_{41}/\gamma_{45} = 2$. (b) Decrease of absorption with $\gamma_{41}/\gamma_{45} = 1/2$.

III. MEASUREMENT OF THE HYPERFINE SPLITTING

A. Apparatus

We use a Coherent 899-01 Titanium Sapphire (Ti:sapph) laser with a linewidth of better than 500 kHz tuned to the D1 line at 795 nm for the first step of the transition. A Pound-Drever-Hall (PDH) lock to the $F=1(2) \rightarrow F=2(3)$ transition in ^{87}Rb (^{85}Rb) in a separate glass cell at room temperature stabilizes the linewidth and keeps the 795 nm laser on resonance. An HP 8640B signal generator acts as the local oscillator for the lock. The 795 nm laser remains on resonance for about 40 minutes, much longer than the time it takes to record a single experimental trace.

A grating narrowed diode laser at 1.3 μm with a linewidth better than 500 kHz excites the second transition. We scan the frequency of the 1.3 μm laser with a triangular shaped voltage ramp from a synthesized function generator at 4 Hz applied to the piezo control of the grating and monitor its frequency with a wavemeter with a precision of $\pm 0.001 \text{ cm}^{-1}$. A fiber-coupled semiconductor amplifier increases the power of the 1.3 μm laser before it goes to a large bandwidth ($\approx 10 \text{ GHz}$) Electro-Optic Modulator (EOM). Another HP 8640B modulates this EOM. Fig. 5 shows a block diagram of the experimental setup.

A thick glass plate splits the 795 nm laser beam into two copropagating beams before going to the glass cell. The power of each beam is approximately $10 \mu\text{W}$ with a diameter of 1 mm. We operate in the low intensity regime to avoid power broadening, differential AC stark shifts and line splitting effects such as the Autler-Townes splitting. Both beams are circularly polarized by a $\lambda/4$ waveplate. A counter propagating 1.3 μm laser beam

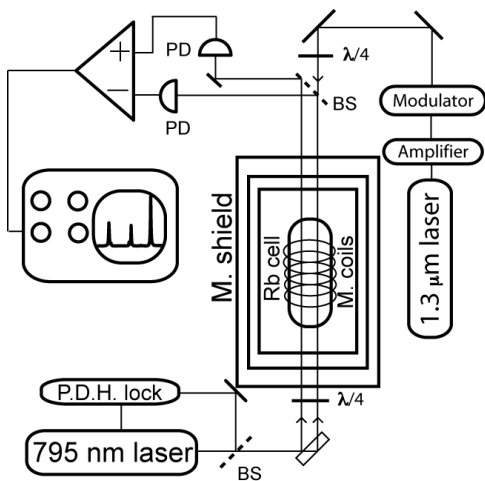


FIG. 5: Block diagram of the experiment. Key for figure PD: photodiode, P.D.H.: Pound-Drever-Hall, M: magnetic, BS: beamsplitter.

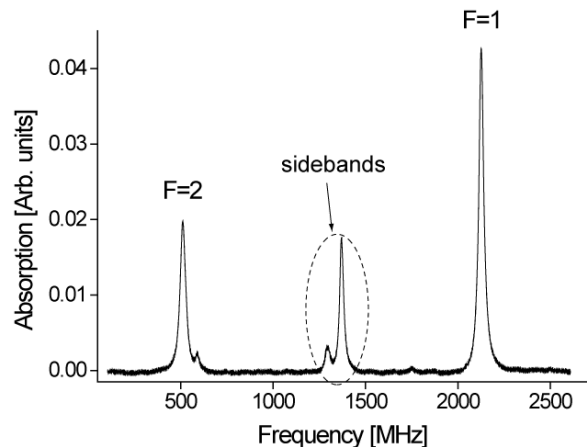


FIG. 6: Absorption profile of the $6S_{1/2}$, $F=1$ and $F=2$ hyperfine states of ^{87}Rb with sidebands. The big sideband belongs to the $F=1$ peak. The small feature on the side of the $F=2$ peak corresponds to the second sideband of the $F=1$ peak. The glass cell is in a magnetic field of 0.37 G.

with a power of 4 mW and approximately equal diameter overlaps one of the 795 nm beams. The lasers overlap to a precision of better than 1 mm along 75 cm. The cell resides in the center of a 500-turn solenoid that provides a magnetic field of 7.4 Gauss/A contained inside a three layered magnetic shield to minimize magnetic field fluctuations [38]. The middle layer has a higher magnetic permeability to avoid saturation effects. The solenoid is 70 cm long and has a diameter of 11.5 cm. We operate under a weak magnetic field ($B \approx 1 \text{ Gauss}$) to work in the Zeeman linear regime.

After the glass cell an independent photodiode detects each 795 nm beam. The outputs of the detectors go to a differential amplifier to reduce common noise. A digital oscilloscope records the output signal for different values of modulation, polarization and magnetic field and averages for about three minutes. The order in which the absorption profiles are recorded is random. During the experimental runs we monitor the current going to the solenoid that provides the quantization axis. A thermocouple measures the changes in temperature inside the magnetic shield ($24 \text{ }^\circ\text{C}$) to within one degree. The optical attenuation for the D1 line at line center is 0.4 for ^{85}Rb and about three times less for ^{87}Rb .

B. Method

We modulate the 1.3 μm laser to add sidebands at an appropriate frequency with a modulation depth (ratio of sideband amplitude to carrier amplitude) that ranges between 1 and 0.1. The sidebands appear in the absorption profile at a distance equal to the modulation from the main features and work as an *in situ* scale (see Fig. 6). We measure their separation as a function of the modulation for values bigger and smaller than half the hyperfine

splitting. We interpolate to zero separation to obtain half the hyperfine splitting (see Fig. 7). This technique transfers an optical frequency measurement to a much easier frequency measurement in the RF range.

The size of the main peaks depends on the coupling strength between transitions; the size of the sidebands (as compared to the main peaks) will be determined by the strength of the transition and also on the number of sidebands simultaneously on or close to resonance. We observe under normal experimental conditions that the laser sidebands are both close to resonance (the lower frequency sideband to the $6S_{1/2}$ $F=1$ and the upper one to the $F=2$ transition) when the carrier is around the half point of the splitting. The stronger of the transitions ($F=1$) depopulates the $5P_{1/2}$ $F=2$ level leaving only a few atoms to excite with the upper sideband, hence the smaller transmission peak for the sideband corresponding to $F=2$.

We have also observed a much richer atomic behavior by changing the laser intensities, polarizations and magnetic field environment of the glass cell. Optical pumping moves the atomic population from one level to another quite efficiently. This is manifest in how the peaks change in magnitude or just switch from an increase of absorption to a decrease (see Fig. 8) just as our very simple theoretical model predicts. These effects point out that a careful control of the environment is necessary for a successful realization of the experiment.

The transfer of population by specific selection of polarization and magnetic environment can also be used to obtain a better experimental signal. There are several options to reach the $6S_{1/2}$ level. From the ground hyperfine states we can do $\Delta F = 0, \pm 1$ transitions. We find that doing the two step excitation in either a $\sigma^+ : \sigma^-$ or $\sigma^- : \sigma^+$ polarization sequence for the 795 nm and $1.3 \mu\text{m}$ lasers, respectively, with a $\Delta F = 1$ for the first step increases the amplitude of the signal. By choosing this polarization sequence we increase the probability of the atom going to the excited state and avoid placing it

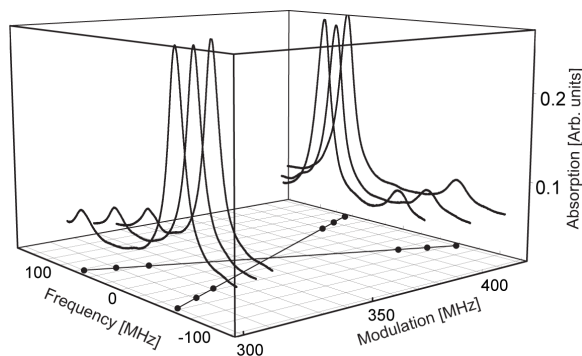


FIG. 7: Experimental traces that illustrate sideband crossing for ^{85}Rb . The larger resonance corresponds to the $F = 2$ level, the smaller one to the $F = 3$ level of the $6S_{1/2}$ state. The dots correspond to the center of the profiles, the point where both lines cross corresponds to half the hyperfine separation.

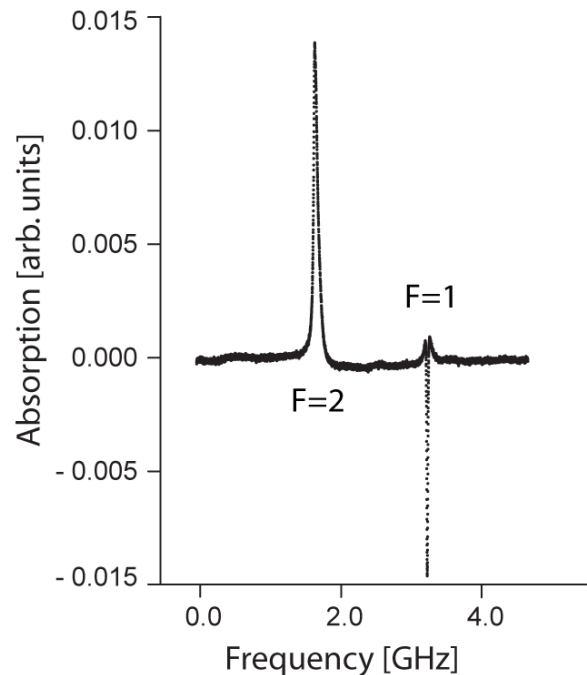


FIG. 8: Experimental trace of absorption of the 795 nm laser for ^{87}Rb showing both increase and decrease of absorption due to optical pumping.

in a non-absorbing state [41].

We place the rubidium cell in a uniform magnetic field collinear with the propagation vectors of both lasers. The magnetic field provides a quantization axis as well as a tool to probe systematic effects. The hyperfine separation is now dependent on the magnetic field strength and the alignment with the laser. We measure the hyperfine splitting for different values of the magnetic field and polarization making sure that the above polarization sequence is always satisfied. We extract the value of the splitting at zero magnetic field from a plot of hyperfine splitting as a function of magnetic field.

C. Systematic effects and results

We study the contributions of several systematic effects that can influence the hyperfine separation measurement. We analyze the peak shape model for the non-linear fit to obtain the separation of the centers of the profiles, scan width and scan rate of the $1.3 \mu\text{m}$ laser, power of the 795 nm and $1.3 \mu\text{m}$ lasers, optical pumping effects, magnetic field effects, and temperature.

A) *Peak shape model and non-linear fit.* The absorption of a Doppler-broadened two level system as a function of laser detuning is a Voigt profile. When a multilevel system is considered it is not trivial to write down the functional form of the absorption of any of the lasers interacting with the system (see for example Refs. [39, 40]). We fit the experimental data to Voigt, Lorentzian and

Gaussian functions to find the line centers and compare the results for consistency.

We use the non-linear fit package of ORIGIN™ to fit the above mentioned profiles to search for model-dependent systematics. ORIGIN™ uses a Levenberg-Marquardt algorithm to minimize the residuals given a specified error. The program has been used in the past by our group to obtain high precision lifetime measurements [37, 42]. We use the resolution limit of the 8 bit analog to digital converter of the scope for these calculations which corresponds to 0.5% of the total scale used. Lorentzian and Gaussian fits have three variable parameters to fit for each peak which correspond to the FWHM, the line center, the area under the curve plus a single offset for both peaks. Voigt profiles have an extra parameter which corresponds to the temperature of the sample. ORIGIN™ gives the error of each parameter which depends on the quality of the data.

Voigt profiles are in very good agreement with the lineshape. The fit yields the low temperature limit of the Voigt profile i.e. a Lorentzian, and hence is in agreement with the linecenter extracted using a Lorentzian profile. This is expected since the contribution of the Doppler ef-

fect on the resonance lineshape should be minimized by the counter propagating laser setup and by an expected group velocity selection arising from the two-step excitation process (“two-color hole burning”). The 795 nm laser will only interact with a small number of group velocities; these groups will be the only ones that will be excited to the $6S_{1/2}$ level by the $1.3 \mu\text{m}$ laser. Line centers extracted from Gaussian fits agree with results from the above mentioned profiles but decay too fast for frequencies far away from the centers. We also fit the data to a convolution of Lorentzian profiles with a rectangular transmission function and an exponential of a Lorentzian to search for systematic errors and to understand better our residues.

All peak shape models give line centers consistent among themselves. All of them have similar structures in the residues within the line width of the resonances (see Fig. 9). We have determined that these features come about from the high sensitivity from deviations from a perfect fit that a difference of two peak profiles has. In other words, by taking the residues we are effectively taking the derivative of a peak profile that will be as sensitive as sharp the linewidth is. To further verify this we take the numerical derivative of the data to search for residual structure that might change our measurement. We fit a straight line to the data that lies within the linewidth and extract when the line crosses zero. The results are consistent with the fits. Close analysis of the derivative in this region reveals no structure.

Of the fitted functions Lorentzians yield the smallest χ^2 . The fitting error of the line centers for all our data for Lorentzian fits range between 15 kHz and 30 kHz. We quote the average of all the fitting errors of our data in Table III. Fig. 9 shows a zoom of the sidebands as well as the residues for a Lorentzian and Gaussian fits. We extract the line centers with both models; the difference in separation for both models is in this case $|x_1 - x_2|_{\text{Lorentzian}} - |x_1 - x_2|_{\text{Gaussian}} = 0.35(68)$ MHz. The reduced χ^2 of the non-linear Lorentzian fit for all our data ranges between 1 and 10 depending on the noise of the signal with a χ^2 average of 2.4 over twenty fits. We do not observe changes in the splitting that depend on the frequency range fitted around the resonances.

The relative angle between both copropagating lasers induces a systematic shift on the absolute frequency the atoms observe due to the appearance of the $\vec{v} \cdot \vec{k}_i$ dependence on absorption where \vec{v} is the velocity of the atom and \vec{k}_i is the wave vector for either laser. This angle dependence on the Doppler shift for our system is almost the same for both our lasers since the cosine of the angle between them differs from one by one part in 10^5 . Furthermore, any residual effect is minimized since we measure frequency differences.

Just like the line shape, analytic expressions for the linewidth are difficult to write down. We perform a numerical simulation of our five level system presented in subsection *D* of the theoretical background in the presence of a room temperature velocity distribution. The

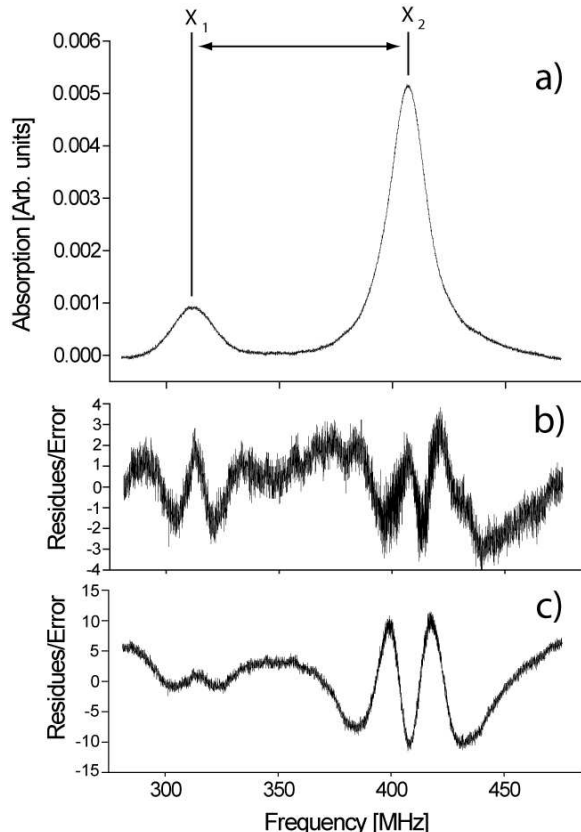


FIG. 9: (a) Scan of the sidebands of the $6S_{1/2}$, $F=1$ and $F=2$ hyperfine states of ^{87}Rb . The fits are not shown for clarity. (b) Normalized residuals of the Lorentzian fit, the reduced χ^2 is 2.13. (c) Normalized residuals of the Gaussian fit, the reduced χ^2 is 23.13.

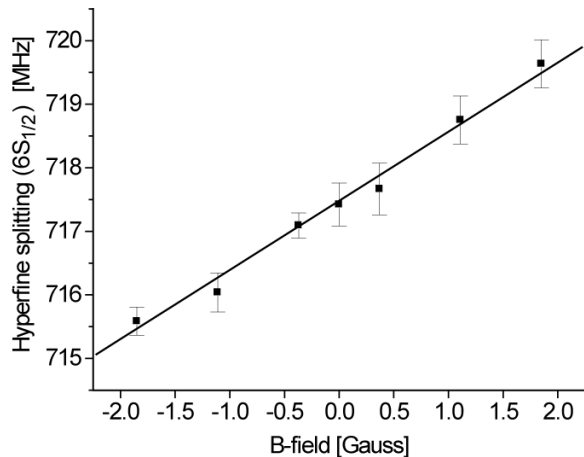


FIG. 10: Zeeman plot of the hyperfine separation of the $6S_{1/2}$ level of ^{85}Rb with both lasers circularly polarized to better than 95% and linear fit.

resonances show linewidths of the order of 30-40 MHz which are in very good agreement with experimental results.

Distortions of the lineshape i.e. asymmetries, depend on the detuning of the 795 nm laser from resonance. These can induce unwanted systematic errors to the measurement. Numerical simulations show, following Ref [8], that the separation of the hyperfine splitting depends negligibly on the detuning from the D1 line. Nevertheless, we look for any asymmetries in the peaks themselves and dependence on the direction of scan during experimental runs. No correlation with these effects is found.

We interpolate to zero from a plot of distance between the center of the sidebands *vs.* the modulation frequency to obtain half the hyperfine separation. The linear regression coefficients in this plots differ from one at the most in 2 parts in 10^4 . Typical errors for the crossovers amount to about 200 kHz.

B) *Scan and linearity of 1.3 μm laser.* Non-linearities in the piezo driving the feedback grating, hysteresis effects as well as a slow thermal drift on the 1.3 μm laser can generate undesired systematics in the measurement. We look for non-linearities by sending the voltage monitor of the piezo to a digital scope with an 8-bit resolution during the experimental runs as well as monitor the absorption peaks for asymmetries. Comparison between absorption peaks for both types of scan (low to high frequency and vice versa) reveals no systematic effects. Analysis of the long term drift of the 1.3 μm laser shows a stability of better than 100 kHz over a 5 min. period which is longer than the time we need to take a single experimental absorption signal.

C) *Power of the 795 nm and 1.3 μm laser.* We look for systematic dependence on the hyperfine splitting on the power of both lasers. We change the power of the 795 nm laser from 4 μW to 40 μW while keeping the power of the 1.3 μm laser constant. Low signal to noise ratio and the observation of the Autler Townes splitting determine the

lower and upper boundaries of this interval, respectively.

The Autler Townes effect predicts a splitting of the middle energy level by the on-resonance first step in a three level system that is proportional to the square root of its intensity [43]. For our typical experimental conditions the splitting should be less than 4 MHz, very small to be resolved with the observed linewidths of the atomic resonances (~ 40 MHz).

The 1.3 μm laser operates very close to its maximum power on normal experimental conditions. The power is distributed among the sidebands and the main carrier depending on the modulation depth. We gradually decrease the power of the 1.3 μm to half its operating value to detect any dependence on the power. We observe no correlation.

D) *Optical pumping effects and magnetic field.* Optical pumping effects are the most delicate of all the systematic effects. Both laser beams are carefully polarized using appropriate $\lambda/4$ waveplates and their polarization checked with a rotating polarizer in front of a detector to better than 95%. The polarization of the lasers as well as their alignment with the magnetic field determine the relative size of the peaks (m_F sublevels) that form the resonances of the $6S_{1/2}$ hyperfine levels. Comparison of absorption profiles for a set polarization sequence for different values of the magnetic field gives qualitative information of the alignment between the magnetic field and the lasers. The positive and negative magnetic field orientations in a perfectly symmetric situation, after a switch of polarization sequence, should yield the same absorption profile. For everyday experimental conditions (around 1 G) we observe no difference between positive and negative magnetic field directions. We see broadening of the profiles at magnetic fields twenty times larger but no asymmetries. Differences start appearing at around 85 Gauss which suggests good alignment between the lasers and the magnetic field as well as good control on polarization of both lasers.

The hyperfine separation *vs.* magnetic field plot provides more quantitative information. Eq. (3) states that the plot should be linear with no discontinuities as we change the value of the magnetic field from positive to negative. Our plots show a smooth transition between negative and positive values of the magnetic field within experimental error. Fig. 10 shows a sample of our data when both lasers are circularly polarized to better than 95%.

We monitor the current of the coil generating the magnetic field to detect any fluctuation in the intensity of the field. We observe small current noise that manifest into fluctuations at most of the order of milligauss.

E) *Temperature.* We analyze the position of the absorption peaks as a function of temperature of the cell to check for related systematic effects such as collision shifts for both isotopes. The temperature of the glass cell is increased from room temperature (23 $^{\circ}\text{C}$) up to 40 $^{\circ}\text{C}$ using a heat tape wrapped around it. While recording data we turn off the heating tape to avoid stray magnetic fields

| Systematic effects | ν_{HF}^{85} [MHz] | ν_{HF}^{87} [MHz] |
|----------------------------------|--------------------------------|--------------------------------|
| Optical pumping effects | ≤ 0.016 | ≤ 0.029 |
| Power of 795 nm laser | ≤ 0.020 | ≤ 0.005 |
| Power of 1.3 μm laser | ≤ 0.011 | ≤ 0.011 |
| Atomic density | ≤ 0.020 | ≤ 0.010 |
| Non linear fit | ≤ 0.028 | ≤ 0.023 |
| B-field fluctuations | ≤ 0.015 | ≤ 0.025 |
| Total Systematic | ≤ 0.047 | ≤ 0.047 |
| Statistical error | 0.100 | 0.160 |
| TOTAL | 0.110 | 0.167 |

TABLE III: Error budget for the hyperfine splitting measurement

generated by the current going through it. The temperature of the glass cell is monitored with a thermocouple inside the magnetic shield with an accuracy of one degree celcius. No dependency on temperature is found.

We have concluded after close analysis of these studies that, to the accuracy of our measurement, Gaussianly distributed statistical fluctuations dominate our experiment (see Table III). The statistical error in the hyperfine splitting, as stated by the standard error of the mean, is 110 kHz for ^{85}Rb and 167 kHz for ^{87}Rb .

Figure 11 shows the values of the magnetic dipole constant for ^{85}Rb for all experimental runs of this work. The final result of each run is determined by an interpolation to zero magnetic field as a function of the current in the solenoid.

Table IV contains the measurements of the hyperfine splitting of the $6S_{1/2}$ level as well as the corresponding values of the magnetic dipole constants for both isotopes.

The precision of our data allows us to observe a hyperfine anomaly. We use the values of Ref. [44] for the ratio $g_1^{85}/g_1^{87} = 0.295055(25)$. This is consistent with the experimental values of Ref. [34]. Using this value and our

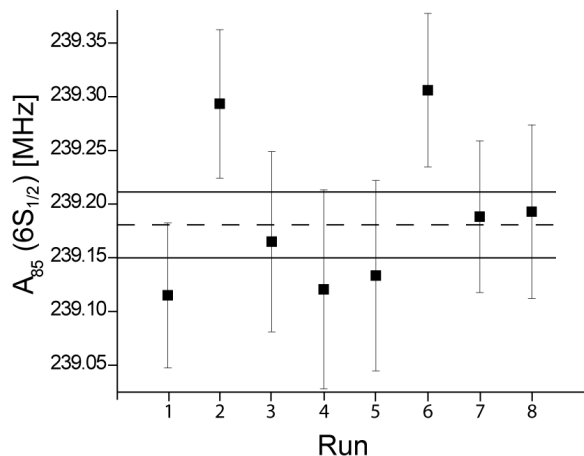


FIG. 11: Results of different runs of the magnetic dipole constants of the $6S_{1/2}$ state of ^{85}Rb . The dashed line corresponds to the mean, the solid lines to the $1\text{-}\sigma$ error.

experimental results in Eq. 6 we obtain a value for the hyperfine anomaly difference of $_{87}\delta_{85} = -0.0036(2)$. This is less than one percent difference, well beyond the current MBPT theoretical calculation accuracy of the hyperfine splittings.

| | ^{85}Rb [MHz] | ^{87}Rb [MHz] |
|------------|------------------------|------------------------|
| ν_{HF} | 717.54(10) | 1615.32(16) |
| A | 239.18(03) | 807.66(08) |

TABLE IV: Hyperfine splittings (ν_{HF}) and magnetic dipole constants for the $6S_{1/2}$ level.

IV. COMPARISON WITH THEORY

We compare in Figs. 12 and 13 the results from this experiment with the previous experimental results of Gupta *et al.* [45] and the theoretical predictions of Safronova *et al.* [9]. The hyperfine anomalies are still not within reach of MBPT so the value of ^{85}Rb comes from considering no hyperfine anomaly.

| | SD [MHz] | SDpT [MHz] | Experiment [MHz] |
|------------|----------|------------|-----------------------|
| $5S_{1/2}$ | 642.6 | 1011.1 | 1011.910813(2) [46] |
| $5P_{1/2}$ | 69.8 | 120.4 | 120.499 (10) [1] |
| $6S_{1/2}$ | 171.6 | 238.2 | 239.18(3) (this work) |
| $6P_{1/2}$ | 24.55 | 39.02 | 39.11(3) [3, 4] |
| $7S_{1/2}$ | 70.3 | 94.3 | 94.658(19) [5] |

TABLE V: Single Double (SD) and partial triple (SDpT) excitation calculated from *ab initio* MBPT in Ref. [9] and experiment magnetic dipole constants for the first $J=1/2$ levels in ^{85}Rb .

Table V shows the values of the magnetic dipole constants using relativistic MBPT [9] with single double (SD) and single double partial triple (SDpT) wave functions and values extracted from measurements of the hyperfine splitting in other electronic states currently in the literature for $J=1/2$ [1, 3, 4, 5, 46]. We have not been able to find in the literature values for higher levels with adequate precision to include them in the figure. The agreement of the theory with the experiment, for $J=1/2$ levels, is well within the 1% level. The SDpT relativistic wave functions do indeed improve the accuracy of the calculations of the single double wave functions.

V. CONCLUSIONS

We have measured the hyperfine splittings of the $6S_{1/2}$ level of ^{85}Rb and ^{87}Rb to a precision of 103 ppm and 153 ppm, respectively. Our measurement is consistent with and decreases the uncertainty of the past measurements [45] by a factor of 63 for ^{87}Rb and by a factor of 30 for ^{85}Rb .

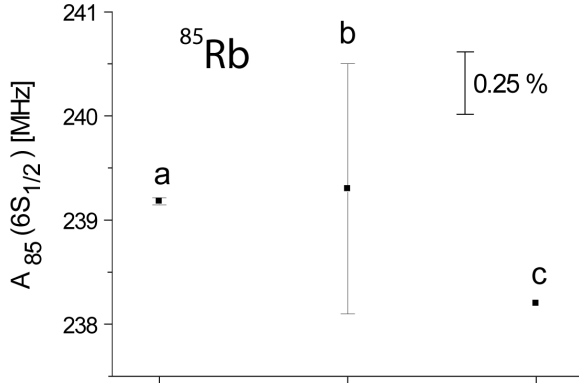


FIG. 12: Comparison between experimental and theoretical results of the magnetic dipole constant of the $6S_{1/2}$ state of ^{85}Rb . The points labeled “a” and “b” correspond to our work and the work of Ref. [45], respectively. Point “c” corresponds to the theoretical prediction of [9].

We are able to extract the hyperfine anomaly with our experimental data and show that precision measurements of the hyperfine structure in atomic states with different radial distributions can give information on the nuclear magnetization distribution. The hyperfine anomaly difference we extract for the $6S_{1/2}$ is ${}_{87}\delta_{85} = -0.0036(2)$. The difference in the anomalies is indeed a factor of thirty larger than the expected BCRS contribution and it comes from the BW effect. Fig. 14 shows that the anomaly measured with the $nS_{1/2}$ levels is the same independent of the principal quantum number as well as the smaller deviation from the point interaction, if any, for the $nP_{1/2}$ levels [1, 3, 4, 5, 12, 46]. Table VI shows the hyperfine anomaly differences for the first $J = 1/2$ levels.

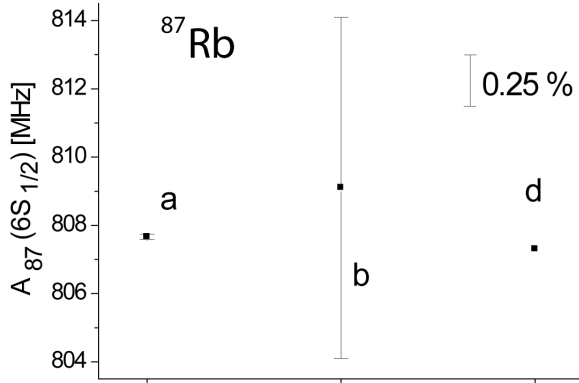


FIG. 13: Comparison between experimental and theoretical results of the magnetic dipole constant of the $6S_{1/2}$ state of ^{87}Rb . The points labeled “a” and “b” correspond to our work and the work of [45], respectively. Point “d” corresponds to the theoretical prediction of Ref. [9]. The value for ^{87}Rb is obtained from the theoretical prediction for ^{85}Rb by considering the hyperfine anomaly as nonexistent.

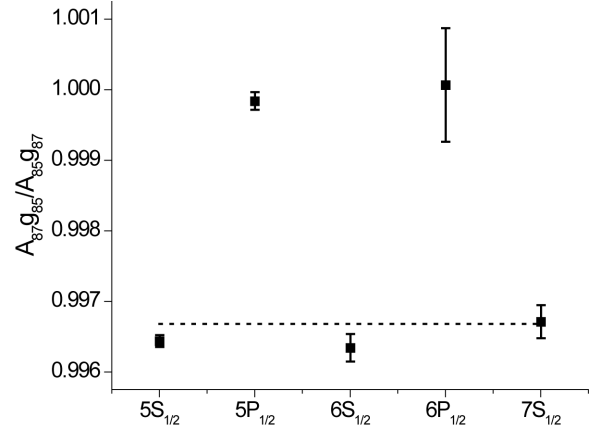


FIG. 14: Hyperfine anomalies of other atomic levels of rubidium along with the value calculated in this measurement. The dashed line corresponds to the theoretical prediction for a diffuse magnetization distribution. See text for references.

| | ${}_{87}\delta_{85}$ |
|------------|--------------------------|
| $5S_{1/2}$ | $-0.00356(8)$ [46] |
| $5P_{1/2}$ | $-0.0001(1)$ [1] |
| $6S_{1/2}$ | $-0.0036(2)$ (this work) |
| $6P_{1/2}$ | $0.0000(8)$ [3, 4] |
| $7S_{1/2}$ | $-0.0032(2)$ [5] |

TABLE VI: Hyperfine anomaly differences ${}_{87}\delta_{85}$ for the first $J=1/2$ levels in rubidium.

The plot and the table confirm that it is the electronic angular momentum and not the principal quantum number that determines the Bohr-Weisskopf effect and the bigger anomaly of the $nS_{1/2}$ levels due to their larger electronic density near the nucleus [27]. These new measurements invite new calculations of atomic properties and constrain nuclear calculations. As the nuclear charge and magnetization distribution are better understood they will further test and refine the calculations which are of crucial importance for parity non-conservation experiments.

Acknowledgments

Work supported by NSF. A.P.G. would like to thank G. D. Sprouse for insightful discussions on nuclear physics and R.T. Willis for assistance with numerical simulations of the atomic system.

-
- [1] G. P. Barwood, P. Gill, and W. R. C. Rowley, *Appl. Phys. B: Photophys. Laser Chem.* 53, 142 (1991).
- [2] V. Gerginov, A. Derevianko, and C. E. Tanner, *Phys.Rev.Lett.* 91, 072501(2003).
- [3] A. Marian, M. C. Stowe, J. R. Lawall, D. Felinto, and J. Ye, *Science* 306, 2063 (2004).
- [4] A. Marian, M. C. Stowe, D. Felinto, and J. Ye, *Phys. Rev. Lett.* 95, 023001 (2005).
- [5] H.-C. Chui, M.-S. Ko, Y.-W. Liu, J.-T. Shy, J.-L. Peng, and H. Ahn, *Opt. Lett.* 30, 842 (2005).
- [6] V. A. Dzuba, W. R. Johnson, and M. S. Safronova, *Phys. Rev. A* 72, 22503 (2005).
- [7] E. Gómez, S. Aubin, L. A. Orozco, and G. D. Sprouse, *J. Opt. Soc. Am. B* 21,2058 (2004).
- [8] J. M. Grossman, R. P. Filler III, T. E. Mehlstäubler, L. A. Orozco, M. R. Pearson, G. D. Sprouse, and W. Z. Zhao, *Phys. Rev. A* 62, 052507 (2000).
- [9] M. S. Safronova, W. R. Johnson, and A. Derevianko, *Phys. Rev. A* 60, 4476 (1999).
- [10] J. S. M. Ginges and V. V. Flambaum, *Phys. Rep.* 397, 63 (2004).
- [11] W. R. Johnson, *Atomic Structure Theory: Lectures on Atomic Physics*, (Springer, New York, NY, 2007).
- [12] A. Pérez Galván, Y. Zhao, L. A. Orozco, E. Gómez, F. J. Baumer, A. D. Lange and G. D. Sprouse, *Phys. Lett. B* 655, 114 (2007).
- [13] W. Pauli, *Naturwissenschaften* 12, 74 (1924).
- [14] E. Back and S. Goudsmit, *Z. Phys.* 43, 321 (1927).
- [15] E. Back and S. Goudsmit, *Z. Phys.* 47, 174 (1928).
- [16] C. S. Wood, S. C. Bennett, D. Cho, B. P. Masterson, J. L. Roberts, C. E. Tanner, and C. E. Wieman, *Science* 275, 1759 (1997).
- [17] C. S. Wood, S. C. Bennett, J. L. Roberts, D. Cho, and C. E. Wieman, *Can. J. Phys.* 77, 7 (1999).
- [18] E. Gómez, S. Aubin, G. D. Sprouse, L. A. Orozco, and D. P. DeMille, *Phys. Rev. A* 75, 033418 (2007).
- [19] H. Kopfermann, *Nuclear Moments* (Academic Press, New York, 1958).
- [20] A. Corney, *Atomic and Laser Spectroscopy* (Clarendon Press, Oxford, 1977).
- [21] L. Armstrong, *Theory of the Hyperfine Structure of Free Atoms* (Wiley-Interscience, New York, 1971).
- [22] M. S. Safronova, C. J. Williams, and C. W. Clark, *Phys. Rev. A* 69, 022509 (2004).
- [23] M. S. Safronova, A. Derevianko, and W. R. Johnson, *Phys. Rev. A* 58, 1016 (1998)
- [24] J. E. Rosenthal and G. Breit, *Phys. Rev.* 41, 459 (1932).
- [25] M. F. Crawford and A. L. Schawlow, *Phys. Rev.* 76, 1310 (1949).
- [26] H. J. Rosenberg and H. H. Stroke, *Phys. Rev. A* 5, 1992 (1972).
- [27] A. Bohr and V. F. Weisskopf, *Phys. Rev.* 77, 94 (1950).
- [28] J. R. Persson, *Eur. Phys. J. A* 2, 3 (1998).
- [29] J. S. Grossman, L. A. Orozco, M. R. Pearson, J. E. Sim-sarian, G. D. Sprouse, and W. Z. Zhao, *Phys. Rev. Lett.* 83, 935 (1999).
- [30] I. Angeli, *At. Data Nucl. Data Tables* 87, 185 (1999).
- [31] C. Thibault, F. Touchard, S. Büttgenbach, R. Klapisch, M. de Saint Simon, H. T. Duong, P. Jacquinet, P. Juncar, S. Liberman, P. Pillet, J. Pinard, J. L. Vialle, A. Pesnelle, and G. Huber, *Phys. Rev. C* 23, 2720 (1981).
- [32] H. H. Stroke, R. J. Blin-Stoyle, and V. Jaccarino, *Phys. Rev.* 123, 1326 (1961).
- [33] T. Yamazaki, T. Nomura, S. Nagamiya, and T. Katou, *Phys. Rev. Lett.* 25, 547 (1970).
- [34] H. T. Duong, C. Ekström, M. Gustafsson, T. T. Inamura, and P. Juncar, P. Lievens, I. Lindgren, S. Matsuki, T. Murayama, R. Neugart, T. Nilsson, T. Nomura, M. Pellarin, S. Penselin, J. Persson, J. Pinard, I. Ragnarsson, O. Redi, H. H. Stroke, and J. L. Vialle, the ISOLDE Collaboration, *Nuc. Instr. and Meth. A* 325, 465 (1993).
- [35] S. Stenholm, *Foundations of Laser Spectroscopy* (Dover Publications, Inc., Mineola, NY, 2005).
- [36] J. E. Simsarian, L. A. Orozco, G. D. Sprouse, and W. Z. Zhao, *Phys. Rev. A* 57, 2448 (1998).
- [37] E. Gomez, F. Baumer, A. D. Lange, G. D. Sprouse, and L. A. Orozco, *Phys. Rev. A* 72, 012502 (2005).
- [38] E. A. Burt and C. R. Ekstrom, *Rev. Sci. Instrum.* 73, 2699 (2002).
- [39] Julio Gea-Banacloche, Yong-qing Li, Shao-zheng Jin, and Min Xiao, *Phys. Rev. A* 51, 576 (1995).
- [40] J. H. Marquardt, H. G. Robinson, and L. Hollberg, *J. Opt. Soc. Am. B* 13, 1384 (1996)
- [41] D. Budker, D. Kimbal, and D. DeMille, *Atomic Physics. An exploration through problems and solutions.* (Oxford University Press, Oxford, 2004).
- [42] E. Gómez, L. A. Orozco, A. Pérez Galván, and G. D. Sprouse, *Phys. Rev. A* 71, 062504 (2005).
- [43] C. Delsart and J. Keller, *J. Phys. (Paris)* 39, 350 (1978).
- [44] N. J. Stone, *At. Data Nucl. Data Tables* 90, 75 (2005).
- [45] R. Gupta, W. Happer, L. K. Lam, and S. Svanberg, *Phys. Rev. A* 8, 2792 (1973).
- [46] E. Arimondo, M. Inguscio, and P. Violino, *Rev. Mod. Phys.* 49, 31 (1977).